catalysts

MDPI

Article

Computational Insights into Ru, Pd and Pt *fcc* Nano-Catalysts from Density Functional Theory Calculations: The Influence of Long-Range Dispersion Corrections

Marietjie J. Ungerer [1,*] and Nora H. De Leeuw [1,2]

[1] School of Chemistry, Cardiff University, Main Building, Park Place, Cardiff CF10 3AT, UK
[2] School of Chemistry, Faculty of Engineering and Physical Sciences, University of Leeds, Leeds LS2 9JT, UK
* Correspondence: ungerermj@cardiff.ac.uk

Abstract: Ruthenium, palladium and platinum fall within the group of noble metals that are widely used in catalysis, especially for the electrocatalytic production of hydrogen. The dominant phase of the bulk Ru metal is hexagonal close-packed (*hcp*), which has been studied extensively. However, significantly less attention has been paid to the face-centred cubic (*fcc*) phases, which have been observed in nanoparticles. In this study, we have carried out density functional theory calculations with long-range dispersion corrections [DFT-D2, DFT-D3 and DFT-D3-(BJ)] to investigate the lattice parameters, surface energies and work functions of the (001), (011) and (111) surfaces of Ru, Pd and Pt in the *fcc* phase. When investigating the surface properties of the three metals, we observed that the DFT-D2 method generally underestimated the lattice parameters by up to 2.2% for Pt and 2.8% for Ru. The surface energies followed the observed trend (111) < (001) < (011) for both Ru and Pd with all three methods, which is comparable to experimental data. For Pt the same trend was observed with DFT-D2 and DFT-D3(BJ), but it deviated to Pt (111) < Pt (011) < Pt (001) for the DFT-D3 method. DFT-D2 overestimated the surface energies for all three Miller Indexes by 82%, 73%, and 60%, when compared to experimental values. The best correlation for the surface energies was obtained with the DFT-D3 and DFT-D3(BJ) methods, both of which have deviate by less than 15% deviation for all surfaces with respect to experiment. The work function followed the trend of Φ (111) < Φ (001) < Φ (011) for all three metals and calculated by all three methods. Five different types of Ru, Pd and Pt nanoparticles were considered, including icosahedral, decahedral, cuboctahedral, cubic and spherical particles of different sizes. The bulk, surface and nanoparticle calculations showed that the DFT-D2 method for Pt overestimated the exchange-correlation, leading to higher energy values that can be contributed erroneously to a more stable structure. The calculations showed that as soon as the surface-to-bulk ratio > 1, the energy per atom resembles bulk energy values.

Keywords: density functional theory; nanoparticles; ruthenium; palladium; platinum; face centred cubic; *fcc*; DFT

Citation: Ungerer, M.J.; De Leeuw, N.H. Computational Insights into Ru, Pd and Pt *fcc* Nano-Catalysts from Density Functional Theory Calculations: The Influence of Long-Range Dispersion Corrections. *Catalysts* **2022**, *12*, 1287. https://doi.org/10.3390/catal12101287

Academic Editors: Omid Norouzi, Pietro Bartocci, Somayeh Taghavi and Shima Masoumi

Received: 27 September 2022
Accepted: 14 October 2022
Published: 21 October 2022

1. Introduction

Hydrogen is a sustainable energy vector, which is set to play a leading role in attaining a net zero carbon economy. Extensive research is carried out into the production of clean H_2, but safe and cost-effective storage and transportation of hydrogen is another major task in the development of a hydrogen economy. Recently, global research efforts have shifted towards storing hydrogen in condensed phases, to increase the density of hydrogen beyond what can be achieved via compression or liquefaction [1]. Liquid organic hydrogen carriers (LOHC) are promising candidates for reversible hydrogen storage and transport [2], whose function is based on a two-step catalytic cycle: (i) loading hydrogen into the LOHC molecule (hydrogenation) and (ii) unloading hydrogen after transport and storage (dehydrogenation).

A crucial aspect in LOHC development is selection of the proper catalytic system for the hydrogenation and dehydrogenation reactions. Various catalysts have been used for both the hydrogenation and dehydrogenation reactions, including precious metals platinum (Pt) [3], palladium (Pd) [4] and ruthenium (Ru) [5], supported on alumina (Al_2O_3), carbide (C) and silica (SiO_2), to achieve chemical routes with high selectivity under sufficiently mild reaction conditions [6]. To understand the performance of Ru-based catalysts, the hexagonal close-packed (*hcp*) phase of Ru, the dominant phase in bulk Ru, has been studied extensively, both experimentally and theoretically using first-principles methods [7,8]. However, significantly less attention has been paid to the face-centred cubic (*fcc*) phase, which has been observed in confined structures such as nanoparticles [9] and has been manufactured using a seeding method [8]. To obtain high catalytic efficiency, metal loading, appropriate support selection, and structural properties (particle size, porosity, active surface area, etc.) are all important characteristics [10]. To this end, the development and optimisation of efficient catalyst systems clearly requires both experimental and theoretical approaches.

Advances in sophisticated computer resources with faster computing capability and state of the art materials simulation methodologies have emerged as important tools in catalysis research owing to their ability to accurately model size-dependent properties and behaviours of nanomaterials [11]. Modern first-principles calculations based on the density functional theory (DFT) are capable of predicting material properties [12], which has made them an indispensable modelling toolkit for scientists to complement experimental research. Even the computational modelling of explicit nanoparticles of various shapes and sizes is now possible with accurate DFT techniques, which allows the rapid development of some catalysts without extensive experimental tests by selecting only the materials that are most suitable for the desired catalytic processes.

One aspect of nanoparticles that we need to consider is that nanosized crystals have a large portion of low coordinated atoms, and the physical properties of nanosized materials (such as the surface energies and morphology) will change as a result of differences in shape and size [13]. The surface energy is a fundamental property of the different facets of a material that is crucial to the understanding of various phenomena, including surface segregation, roughening, catalytic activity, and the crystal's equilibrium shape. Such surface phenomena are especially important at the nanoscale, where the large surface area to volume ratios lead to properties that are significantly different from the bulk. In this work, we present the calculated surface energies and work functions of the extended (001), (011) and (111) Miller index surfaces of the *fcc* phase of Ru, Pd and Pt. Furthermore, we have also explicitly calculated the properties of five different nanoparticles, i.e., icosahedral, decahedral, cuboctahedral, cubic and spherical particles, in a range of 12 to 665 atoms.

2. Computational Methods

2.1. Calculation of Surfaces

The Vienna Ab Initio Simulation Package (VASP) [14–17] version 5.4.1 was used to simulate the bulk and surfaces of the periodic Ru, Pd and Pt metal structures. In all calculations, the projector augmented wave (PAW) [18,19] pseudopotential approach was used to describe the interactions between the valence and core electrons. The core electrons were defined up to and including 4s, 4p and 5p orbitals for the Ru, Pd and Pt atoms, respectively. As such, 10 valence electrons are calculated for both Pt and Pd, but Ru needs to be considered in a different manner. Ru can form compounds in multiple oxidation states, from −2, 0, and +1 to +8. For that reason, not only the $5s^1$ electrons are active in reactions, but all electrons in the $4p^6$ $4d^7$ $5s^1$ need to be considered, i.e., 14 valence electrons in total, which does increase the computational cost. The exchange-correlation approximation was included with the Perdew-Burke-Ernzerhof (PBE) [20] functional within the generalised gradient approximation (GGA). To establish the best fit with experimental data, three approximations were considered to account for the long-range dispersion interactions as observed in similar systems, i.e., the DFT-D2 method by Grimme [21], the

zero damping DFT-D3 method by Grimme [22], and DFT-D3(BJ) method by Grimme with Becke-Johnson damping [23]. Plane waves were included with the recommended cut-off of 400 eV. The conjugate gradient technique was adopted for all geometry optimisations and to ensure an electronic entropy of less than 1 meV·atom^{-1}, whereas a smearing of 0.05 eV with the Methfessel-Paxton scheme order 1 [24] was used to determine the partial occupancies during geometry optimisation. The final static simulations were obtained with the tetrahedron method with Blöchl corrections [25] to ensure accurate total energies, charges and densities of states, where the electronic and ionic optimisation criteria were set at 10^{-5} eV and 10^{-2} eV·Å^{-1}, respectively.

The $Fm\bar{3}m$ crystal structure was used to construct the bulk structures of Ru [26], Pd [27] and Pt [28] within a primitive face-centred cubic (*fcc*) cell. The *k*-point mesh for these calculations was a Γ-centred 17 × 17 × 17 Monkhorst-Pack mesh [29]. The resulting *fcc* lattice constants were 3.778, 3.886 and 3.924 Å, for Ru, Pd and Pt, respectively, which correlate with the experimental values of 3.87 [30], 3.89 [27] and 3.925 Å [31,32], respectively. The low Miller index (001), (011) and (111) surfaces were created with the METADISE code [33]. Periodic p(3 × 3), p(3 × 3) and p(4 × 4) supercells were constructed, respectively, each with four layers and a 15 Å vacuum space to ensure that no interaction would occur between the surfaces in neighbouring simulation cells as a result of the 3-dimensional boundary conditions. All three surfaces are bulk-terminated 2 × 2 structures with four atomic layers, with the surface simulation cells containing 72, 48 and 64 atoms, respectively. The Brillouin zone was sampled by a Γ-centred 7 × 7 × 1 Monkhorst-Pack *k*-point grid. During the optimisation of the surfaces, the bottom two layers of the supercells were frozen in their bulk locations, with the remaining two layers allowed to move until the set energy criteria were met. Even though Pt and Pd do not have unpaired electrons, spin polarisation was considered during these surface calculations, as future work will also include base metal dopants like Ni and Co, for which this would be necessary.

The unrelaxed (Υ_u) and relaxed (Υ_r) surface energies were determined using Equations (1) and (2), respectively:

$$\Upsilon_u = \frac{E_{slab,u} - N_{Pt,slab}E_{Pt,\,bulk}}{2A_{slab}} \quad (1)$$

$$\Upsilon_r = \frac{E_{slab,\,r} - N_{Pt,slab}E_{Pt,\,bulk}}{A_{slab}} - \Upsilon_u \quad (2)$$

where $E_{slab,\,u}$,$E_{slab,\,r}$ and $E_{Pt,\,bulk}$ are the energies of the unrelaxed slab, the half-relaxed slab and the bulk, respectively. $N_{Pt,slab}$ and A_{slab} represent the number of Pt atoms in the slab and the surface area of the slab, respectively. The percentage of relaxation (R) was calculated as the difference between the unrelaxed and relaxed surface energies, divided by the unrelaxed surface energy, multiplied by 100.

Wulff morphologies [34] were constructed using the Wulffpack program [35] The equilibrium Wulff crystal is constructed, assuming that the distance of the crystal face (d_{001}, d_{011}, d_{111}) to the centre of the nanoparticle is proportional to their surface free energies as:

$$\frac{d_{001}}{\sigma_{001}} = \frac{d_{011}}{\sigma_{011}} = \frac{d_{111}}{\sigma_{111}} \quad (3)$$

2.2. Calculation of Nanoparticles

To investigate the nanoparticles, we have used OpenMD (v.2.6) [36], which is an open-source molecular dynamics engine that is capable of efficiently simulating nanoparticles using force fields. The Sutton-Chen [37] potentials have been used to study a wide range of phenomena in metals; they include a repulsive pairwise potential that accounts for interactions of the pseudo-atom cores and a many-body potential that models the interactions between the valence electrons and the cores of the pseudo-atoms. The Sutton-Chen potential was parameterized by Qi et al. [38] via empirical and ab initio calculations to match structural features of the *fcc* crystal. As we considered *fcc* metals, the Sutton-Chen

forcefield [37] was used to account for the Pd and Pt atoms and modified to account for the Ru [39,40] interatomic forces, atomic mass, valence electrons and lattice parameters. OpenMD was used to construct nanoparticles of various sizes and geometries, including icosahedral, decahedral, cuboctahedral, cubic and spherical particles. The resulting coordination files from OpenMD were next used within the VASP software to obtain the optimum geometries and energies.

To ensure that the obtained nanoparticle data can be compared to the bulk and surface calculations, the computational settings were kept the same. Again, we utilised the GGA PBE functional [20] with the three approximations, DFT-D2 [21], DFT-D3 [20], and DFT-D3(BJ) [23] to account for the long-range dispersion interactions. Plane waves were included with the recommended cut-off of 400 eV. Each nanoparticle was modelled in a periodic box of non-equivalent dimensions, i.e.,12 × 13 × 14 Å with at least 10 Å vacuum space in all directions to ensure negligible interaction with neighbouring cells. For both the geometry optimisations and energy calculations, Gaussian smearing [24] of 0.05 eV was used with a Γ-centred Monkhorst-Pack [29] *k*-point mesh of 1 × 1 × 1. None of the nanoparticles were computed with symmetry constraints, but for increased accuracy, dipole corrections were added in all directions. The final static simulations were obtained with the tetrahedron method with Blöchl corrections [25] to ensure accurate total energies, charges and densities of states, where the electronic and ionic optimisation criteria were set at 10^{-5} eV and 10^{-2} eV·Å^{-1}, respectively.

All the graphics for the surfaces and nanoparticles shown here were obtained with the VESTA (Visualization for Electronic and STructural Analysis) code v.3.5.5 [41].

3. Results and Discussion

3.1. Ruthenium, Palladium and Platinum Surfaces

To optimize the geometry of the (001), (011), and (111) surfaces of Ru, Pd and Pt, three different long-range dispersion approximations were tested, including (i) the DFT-D2 method by Grimme, [21] (ii) the zero damping DFT-D3 method by Grimme, [22] and (iii) the DFT-D3 method with Becke–Johnson damping [23]. It is known from previous work with Pt [42] that the DFT-D2 method overestimates the exchange correlation for electrons, leading to an underestimated lattice parameter for Pt and overestimated surface energy. Other authors have also recommended to use DFT-D3 and higher accuracies for metallic systems [43]. However, owing to the fast calculation time, it was deemed useful to have a full set of data that also included the use of DFT-D2 for all three metals for the bulk, surface and nanoparticle calculations.

Figure 1 shows the three mayor Miller index (001), (011) and (111) surfaces considered in this work. The *fcc* arrangement was used for Ru, Pd and Pt, resulting in flat smooth (001) and (111) structures and a corrugated or grooved (011) metal surface. As these are periodic systems, each surface has a 15 Å vacuum space above the surface to avoid interaction with next unit cell. It was shown [42,43] that long-range dispersion corrections influence various parameters of a modelled surface, including the lattice parameter and surface energy.

Listed in Table 1 is the bulk energy (E_{bulk}) and lattice parameters (a) for the bulk system, unrelaxed (γ_u) and relaxed surface energies (γ_r), surface areas (A) and work function (Φ), calculated for the Ru, Pd and Pt (001), (011) and (111) surfaces, using the three different long-range dispersion correction methods.

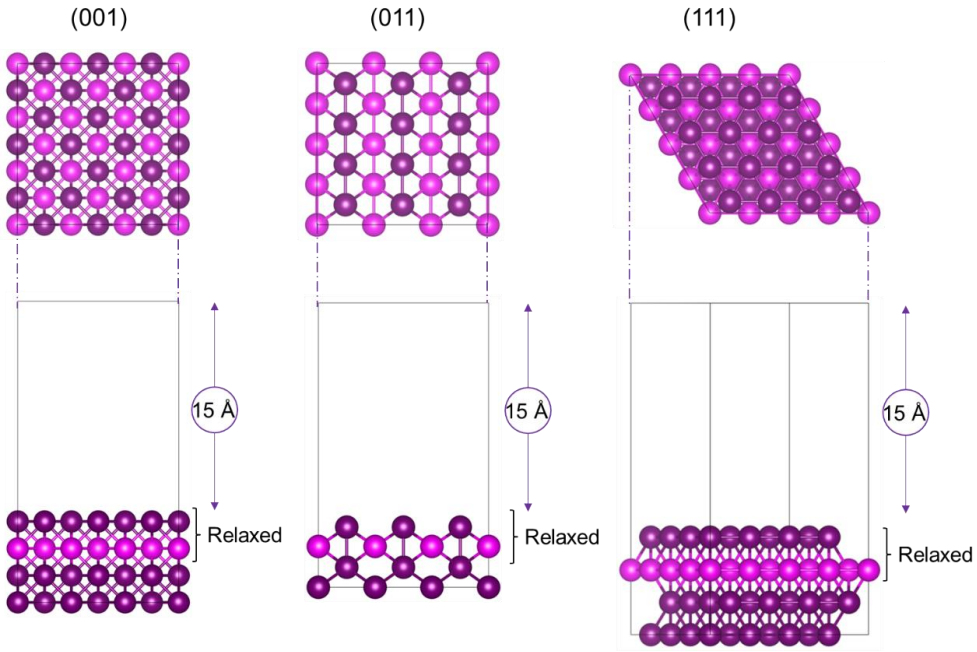

Figure 1. Top and side views of the (001), (011) and (111) surfaces constructed for Ru, Pd and Pt. All metal atoms are shown purple in colour throughout the paper, with the second layer in a lighter colour to distinguish between top layer and subsequent layer atoms.

Table 1. Bulk energy (E_{bulk}) and lattice parameters (a) for the bulk system, unrelaxed (γ_u) and relaxed surface energy (γ_r), surface areas (A) and work function (Φ) was calculated for Ru, Pd and Pt (001), (011) and (111) surfaces, with different long-range dispersion corrections DFT-D2, DFT-D3 and DFT-D3(BJ) method.

	Ruthenium				Palladium				Platinum			
	DFT-D2	**DFT-D3**	**DFT-D3(BJ)**	**Other Work**	**DFT-D2**	**DFT-D3**	**DFT-D3(BJ)**	**Other Work**	**DFT-D2**	**DFT-D3**	**DFT-D3(BJ)**	**Other Work**
E_{bulk} (eV/atom)	−9.83	−9.64	−9.74		−5.90	−5.85	−5.93		−8.05	−7.01	−7.01	
a (Å)	3.763	3.777	3.778	3.818 [44], 3.87 [30]	3.889	3.886	3.886	3.949 [44], 3.89 [27]	3.837	3.917	3.924	3.924 [31,32]
(001)												
γ_u (J.m^{-2})	3.77	3.75	3.65		2.30	2.31	2.28		4.52	2.79	2.73	
γ_r (J.m^{-2})	3.71	3.67	3.58	2.99 [44]	2.30	2.30	2.32	2.15 [45]	4.19	2.79	2.73	1.81 [46]
A (Å^2)	127.48	128.40	128.46		135.94	135.93	135.93		132.50	138.10	138.60	
Φ (eV)	5.18	5.05	5.08	4.85 [47]	5.16	5.06	5.06	5.08 [45], 5.65 [48]	5.81	5.77	5.58	5.66 [46]
(011)												
γ_u (J.m^{-2})	3.95	3.71	3.83		2.44	2.42	2.36		4.31	2.77	2.86	
γ_r (J.m^{-2})	3.81	3.55	3.67	2.77 [44]	2.41	2.41	2.34	2.30 [45]	4.19	2.70	2.79	1.85 [46]
A (Å^2)	120.18	121.05	121.12		128.16	128.16	128.16		124.92	130.20	130.67	
Φ (eV)	4.21	4.20	4.14	4.28 [47]	5.08	5.07	5.06	5.13 [45], 5.20 [48]	5.45	5.53	5.55	5.26 [46]
(111)												
γ_u (J.m^{-2})	3.30	3.20	3.11		2.17	2.15	2.14		3.96	2.18	2.34	
γ_r (J.m^{-2})	3.28	3.18	3.08	2.37 [44], 3.04 [49]	2.15	2.14	2.13	1.90 [45], 2.05 [50]	3.92	2.18	2.33	1.49 [46], 2.49 [51]
A (Å^2)	98.13	98.83	98.89		104.64	104.64	104.64		102.00	106.31	106.69	
Φ (eV)	5.19	5.19	5.23	4.94 [47], 4.71 [52]	5.18	5.18	5.18	5.53 [45], 5.90 [48]	5.84	5.77	5.71	5.69 [46]

All three methods gave similar result for the lattice parameters of Ru, that were underestimated by between 2.6 and 2.8% from the experimental value of 3.87 Å [30]. In the case of Pd, the lattice parameters correlated within 0.01 Å of the experimental value of 3.89 Å [27]. As already mentioned, the Pt lattice parameter was underestimated by 2.2% for

the DFT-D2 method but was within 0.1% for the DFT-D3 and DFT-D3(BJ), when compared to the experimental value of 3.924 Å [31,32].

The surface energies of Ru followed the trend Ru (111) < Ru (001) < Ru (011) for all three methods, although they are higher by about 1 eV compared to the reported literature values. This apparent discrepancy could be due to the fact that not all computational models include the dispersion corrections, leading to very different surface energy values reported in the literature [44]. For example, for all three Ru surfaces the DFT-D2 method leads to a higher value. The surface energies of Pd followed the same trend Pd (111) < Pd (001) < Pd (011) for all three methods. Compared to the reported surface energies, these energies deviate by less than 0.2 eV from literature values, even in the case of DFT-D2, which, however, still gives the highest value.

For Pt, the surface energy trend from the DFT-D2 and DFT-D3(BJ) methods was again Pt (111) < Pt (001) < Pt (011), but from DFT-D3 it became Pt (111) < Pt (011) < Pt (001). In terms of surface energies, all methods confirmed the lowest surface energy for Pt (111), followed by the other two surfaces. Again, the DFT-D2 method overestimated the energies for all three surfaces by 82%, 73%, and 60%, respectively. The best correlation for surface energies was with DFT-D3 and DFT-D3(BJ) methods, both of which deviate by less than 15% for all the surfaces with respect to experiment [51].

The work function, a descriptor inversely related to chemical reactivity, was calculated for the (001), (011), and (111) surfaces. However, the work function alone cannot be used to predict reactivity, as it is dependent on the surface properties as well as temperature [53]. In the case of Ru, the work function follows the same trend as the surface energies Φ (111) < Φ (001) < Φ (011). The Φ (011) correlates well with other modelled data, but for the (001) and (111) it deviates by as much as 0.5 eV. This apparent discrepancy could be due to the fact that it is notoriously difficult to find pure *fcc* Ru surfaces and most surfaces or nanoparticles show some reconstruction to *hcp* [54], which then influences the measured work function. There were no major reconstructions to indicate that our *fcc* model was meta-stable and no suggestion in the bulk relaxation of a partial phase change to "*hcp*-like" packing order. In the case of Pd, it follows a similar trend for all three methods Φ (111) < Φ (001) < Φ (011) and correlates with literature values. For Pt, it was determined that removing an electron would be easiest from the (111) surface, followed by the (001) and (011) surfaces, which trend is also reported in the literature [46], although the data were dependent on the surface area and modelling approximation used. Overall, in the case of the work function, it seems that all three methods gave similar results for each surface and that the dispersion correction plays a more significant role in calculating the lattice parameter and surface energies.

The surface energies from Table 1were used in the Wulff construction method [34] to construct predicted nanoparticle morphologies, where we can visualize which surfaces are more stable and most likely to be present in experimental nanoparticles. Table 2 shows the resulting Wulff morphologies for Ru, Pd and Pt according to the three DFT protocols used. Overall, all three major surfaces are expressed in the nanoparticles, producing a rhombo-cuboctahedron structure with 8 truncated triangular (111) faces, 12 truncated (011) faces, and 6 square (001) faces. We can see that the Ru (111) surface will be present up to 72%, followed by the (001) and (011) surfaces to a lesser extent. A similar trend is observed for both Pd and Pt, i.e., that the (111) surface would be present for reactions to take place. Interestingly, when using the DFT-D3 method, the (011) surfaces does not seem to be expressed in Pt. In an experimental study by Lee et al. [55] it was seen that colloidal particles of Pt preferentially expressed the (001) and (111) facets. However, all three low Miller index surfaces appeared to varying extent in the nanoparticles when the temperature was changed during the experiment.

Table 2. Wulff morphologies constructed from surface energy for the DFT-D2, DFT-D3 and DFT-D3(BJ) method for Ru, Pd and Pt.

	DFT-D2	%	DFT-D3	%	DFT-D3(BJ)	%
Ru						
{111}	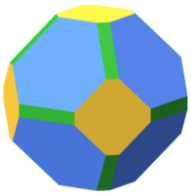	64.9	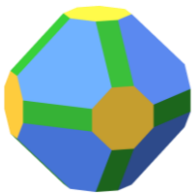	57.2	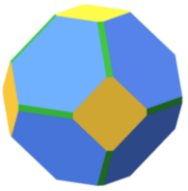	72.5
{001}		24.1		20.4		21.7
{011}		10.9		22.4		5.8
Pd						
{111}	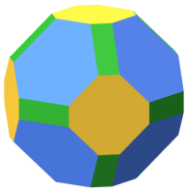	54.6	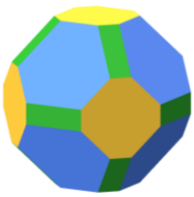	55.0	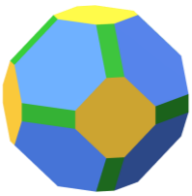	58.4
{001}		29.4		28.9		27.8
{011}		16.0		16.1		13.7
Pt						
{111}	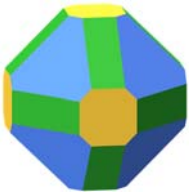	45.9		87.1	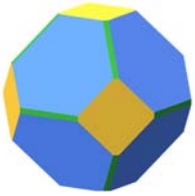	74.3
{001}		18.9		12.9		20.9
{011}		35.2		-		4.8

3.2. Nanoparticles

Five different nanoparticles were considered, including icosahedral, decahedral, cuboctahedral, cubic and spherical particles, as depicted in Figure 2. The first nanoparticle considered was the icosahedral shape. The name comes from the ancient Greek words εἴκοσι (eíkosi), which means 'twenty' and ἕδρα (hédra) 'seat', indicating that an icosahedron has 20 faces of equilateral triangles; they meet in 30 edges and 12 vertices. The triangle faces consist of (111) surfaces. For each of these nanoparticle structural shapes, the nanoparticle is built up of a certain number of atoms that correspond to the optimum stable configurations; these numbers are usually called the magic numbers (G_m) [56]. Mackay [57] found that for icosahedral structures the geometrical packing would follow the order: G_m = 1, 13, 55, 147, 309, 561, which correlates exactly with our calculated structures. We omitted the structure with one atom (G_m = 1) as this does not fall within our definition of a nanoparticle. Considering the first icosahedral nanoparticle (Figure 2: G_m = 13) it can be seen that the triangle surfaces have three atoms, with two atoms on each edge. To obtain the next size a complete layer of atoms is added, resulting in triangle faces with three atoms on the edge (G_m = 55), followed by four, five and six edge atoms for G_m = 147, 309 and 561, respectively. Interestingly, the nanoparticles consisting of Pt and Pd are very similar in size, with Ru being slightly larger. In a previous paper [42,58] on metal bulk structures and surfaces, Pt atoms moved into the bulk from the surface, leading to contraction of atoms which could explain the smaller nanoparticle sizes.

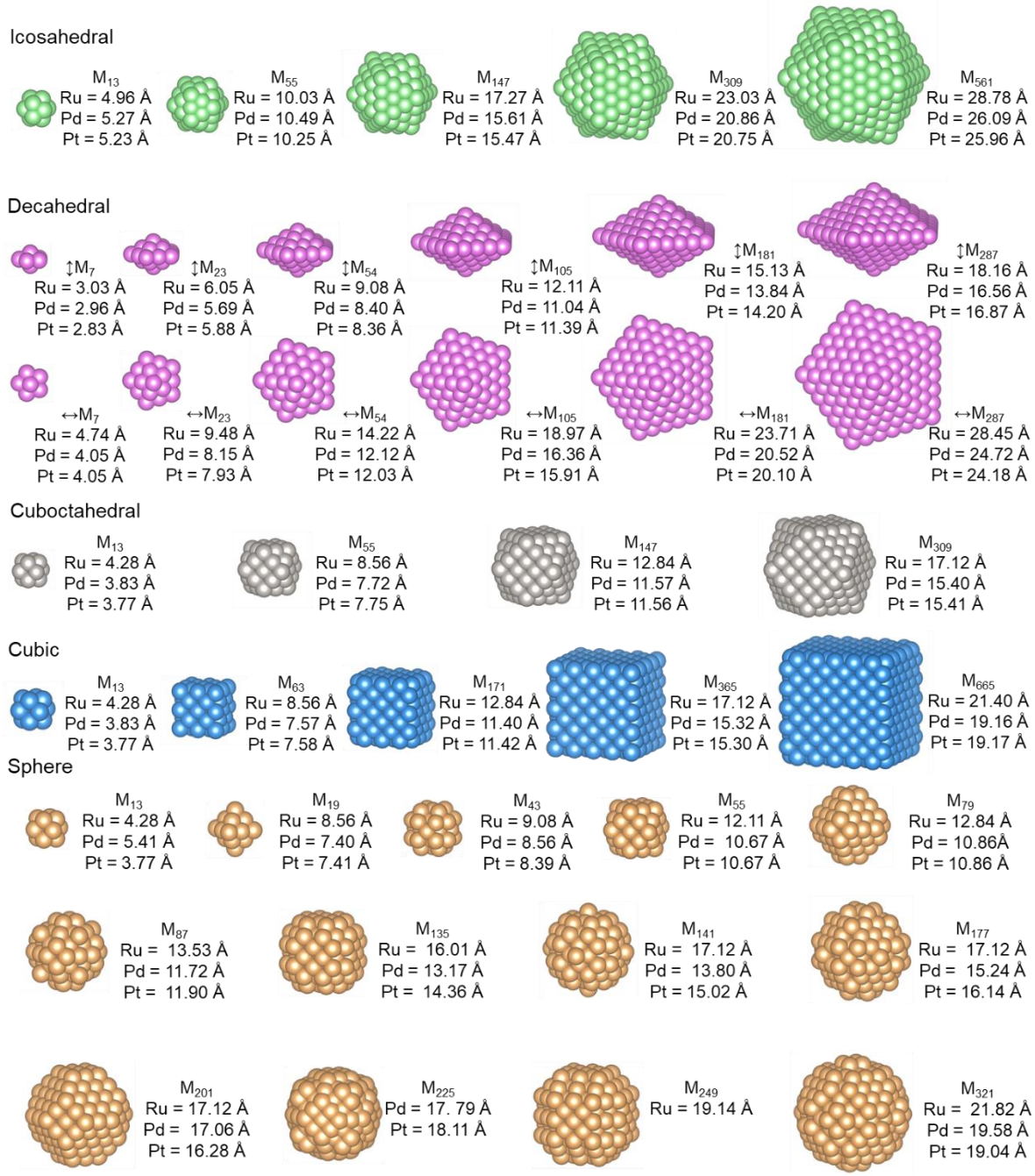

Figure 2. Various sizes and shapes of the stable *fcc* nanostructures for Ru, Pd and Pt, including icosahedral, decahedral, cuboctrahedral, cubic and spherical particles.

The second nanoparticle, the decahedral particle, is a polyhedron with 10 faces. In this class, there are 32,300 topologically distinct decahedra [59,60], and none are regular, so this name does not identify a specific type of polyhedron except for the number of faces. In our case, we constructed various sizes of a pentagonal dipyramid with 5 faces on two distinct sides of the polyhedron, forming 10 equilateral triangles with 15 edges and 7 vertices. In this case, the geometrical packing follows the order: G_m = 1, 7, 23, 54,105, 181 and 287 as each complete shell was added. Similar to the icosahedral shapes, here the Pt and Pd have a very similar size with Ru again being slightly larger.

In both icosahedral and decahedral nanoparticles, all the faces were triangles. However, for the third nanoparticle shape, the cuboctahedral particle has a truncated cubic

structure with 6 square and 8 triangle faces, 24 identical edges and 12 identical vertices, with 2 triangles and 2 squares meeting at each [61]. The square faces have a (001) surface, while the triangle faces have (111) surfaces. Due to the cubic nature, with each successive shell the atom numbers nearly double, G_m = 13, 55, 147 and 309. Similarly, the fourth shape considered was the cubic nanoparticle with 6 square (001) faces, 12 edges and 8 vertices. Five sizes were considered: G_m = 13, 63, 171, 365 and 665.

Finally, the fifth shape was the spherical nanoparticle. Due to the *fcc* packing order, no true spherical shape was obtained and most structures are a combination of icosahedral and cuboctahedral shapes, which has also been reported before, especially in gas phase molecules [62,63]. Sloane and Teo [64] proposed drawing a spherical structure within a perfect crystal lattice, where all atoms contained within the sphere constitute a spherical cluster. Therefore, each successive shell has irregular numbers as shown in Figure 2: G_m = 1, 13, 19, 43, 55, 79, 87, 135, 141, etc. The surfaces here are mostly (001) and (111), although some sizes, for example the M_{249} as only expressed for Ru, have a truncated cuboctahedron shape with (001), (011) and (111) surfaces.

The most stable configurations for Ru, Pd and Pt icosahedral nanoparticles of increasing sizes, obtained using all three DFT-D2, DFT-D3 and DFT-D3(BJ) methods, are shown in Figure 3 in terms of energy per atom versus the number of atoms. For all three metal types and all three calculation methods, the general trend was that the larger values (more negative) were calculated as the particle size increased, indicating a more stable nanostructure. Small nanoparticles have a substantial fraction of their atoms at the surface and as the particle increases in size, more bulk atoms are created. This high surface area to volume ratio is an important factor in many of the physical properties of nanoparticles, including their reactivity. Atoms at the surface are under-coordinated, and because breaking bonds costs energy, surface atoms always have higher energies than atoms in the bulk [65], regardless of whether the bonding is covalent (as in a metal), ionic (in a salt), or non-covalent (in a liquid such as water).

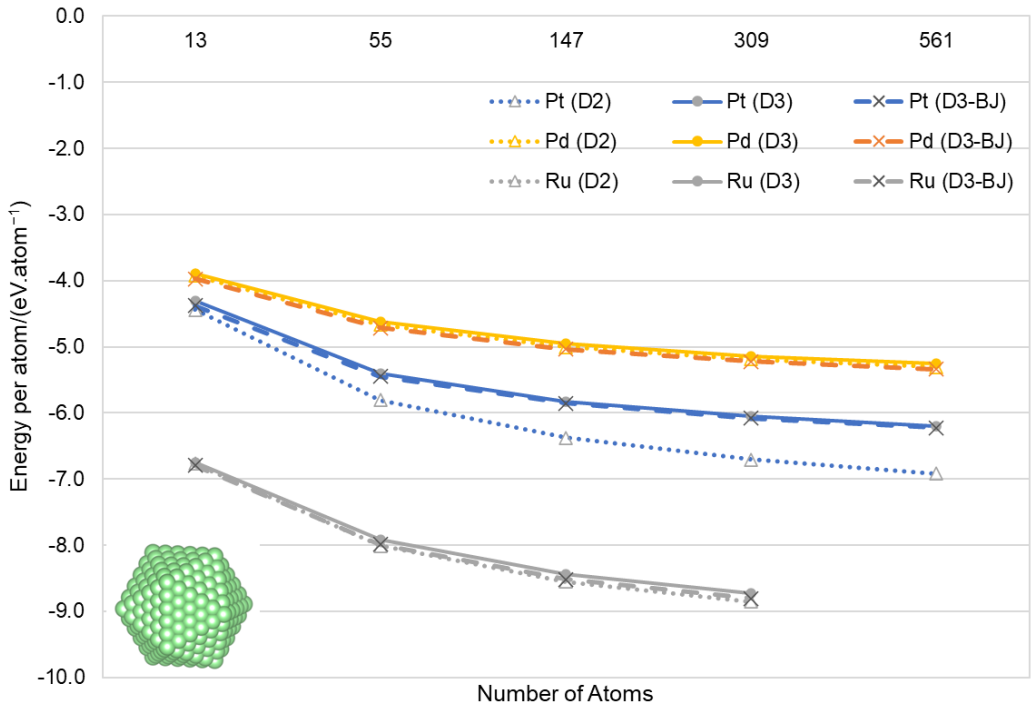

Figure 3. Energy per atom as a function of size for icosahedral Ru, Pd and Pt nanoparticles calculated with the three modelling methods, DFT-D2, DFT-D3 and DFT-D3(BJ).

The smallest icosahedral nanoparticle has 12 surface atoms and 1 bulk atom (ratio of 12/1), compared to the next size ratio of 3.23 for G_m = 55 (42 surface atoms to 13 bulk

atoms), followed by 1.67 (92/55), 1.10 (162/147) and 0.82 (252/309) for G_m = 147, 309 and 561, respectively. The largest nanoparticle considered, G_m = 561 is the first particle where more bulk atoms are present and thus the energy per atom here is comparable to the bulk energy calculated for each metal in Table 1. Comparing the three computational methods (DFT-D2, DFT-D3 and DFT-D3(BJ)), both Pd and Ru obtained similar results for all the nanoparticle sizes calculated. Extrapolating to larger nanoparticles, the energy per atom for Pd reaches higher values than −5 eV/atom, which correlates with the bulk calculations shown in Table 1. Due to computational costs and thus size constraints for the VASP calculations, we were unable to obtain the Ru G_m = 561 structures. Extrapolating the obtained data in Figure 3, we would expect larger Ru nanoparticles to have energy per atom values of between −8 and −9 eV per atom. In the case of Pt, the DFT-D2 method deviates from the others, showing much larger energy values. One might expect this method to produce stable structures based on the large, calculated energy values, but in this case it is erroneous. Table 1 shows the discrepancy between DFT-D2 and DFT-D3 for not only the bulk calculations, but also the surface energy calculations, which are therefore also present in the nanoparticle calculations. The DFT-D2 method overestimates the exchange correlation term for all the electrons in this system (as reported before [42,66]) and as the nanoparticle increases in size, this energy deviation increases too.

The energies as a function of increasing sizes of the decahedral nanoparticles of Ru, Pd and Pt, calculated by the three modelling methods, DFT-D2, DFT-D3 and DFT-D3(BJ), are shown in Figure 4. Similar to the icosahedral structures, the decahedral particles show the energy per atom to increase as the size increases. When calculating the surface-to-bulk atom ratio, we again see a decreasing trend of 6.00, 2.29, 1.35, 0.94, 0.72 and 0.59 for G_m = 7, 23, 54,105, 181 and 287, respectively. In this shape, the number of bulk atoms already exceeds the surface atoms at G_m = 105. Similar to the icosahedral data, all three calculation methods gave similar results for Pd and Ru, with the DFT-D2 method deviating for Pt. Extrapolating the results to larger nanoparticles, the energy per atom reaches values over −5 eV/atom for Pd, −6 eV/atom for Pt and −8 eV/atom for Ru, which correlate with the bulk calculations shown in Table 1.

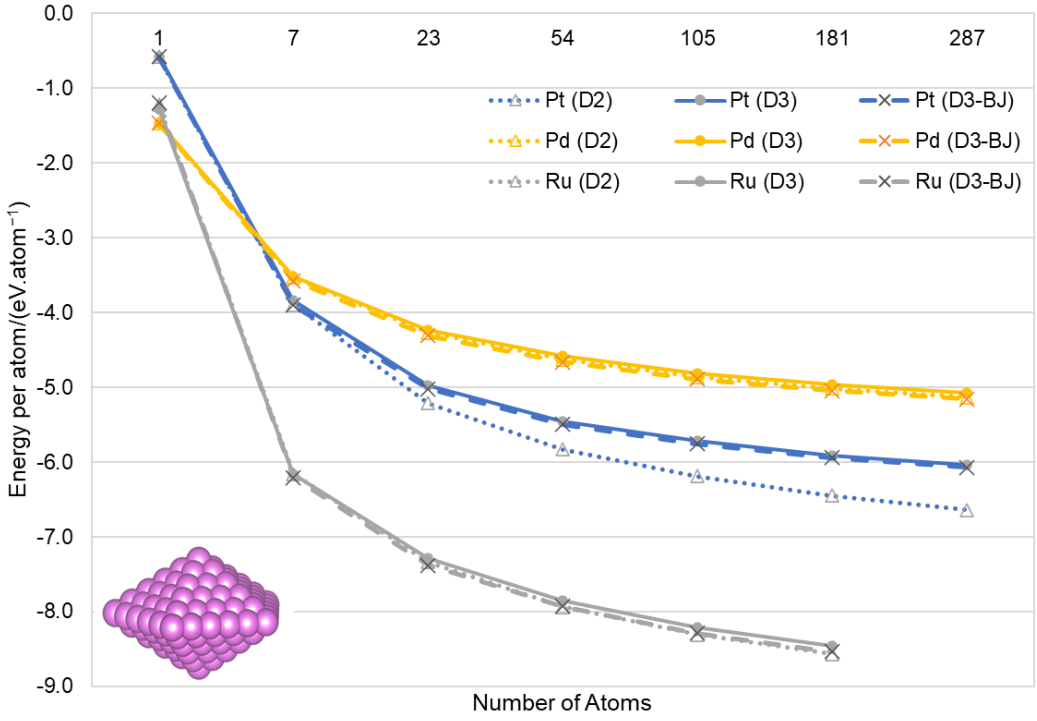

Figure 4. Energy per atom as a function of size for decahedral Ru, Pd and Pt nanoparticles calculated with the three modelling methods, DFT-D2, DFT-D3 and DFT-D3(BJ).

The data for the energies per atom for the cuboctahedral Ru, Pd and Pt nanoparticles of increasing sizes are shown in Figure 5. The data follow similar trends to the icosahedral and decahedral structures, where the energy per atom increases as the size increases. Calculating the surface-to-bulk atom ratios, we again see a decreasing trend of 12.00, 3.23, 1.67 and 1.10 for G_m = 13, 55, 147 and 309, but for this shape, the number of bulk atoms did not exceed the surface atoms within the size range considered. Similar to the icosahedral data, all three calculation methods gave similar results for Pd and Ru, with the DFT-D2 method deviating again for Pt. Extrapolating the energies to larger nanoparticles indicates that the energy per atom reaches values above −5 eV/atom for Pd, −6 eV/atom for Pt and −8 eV/atom for Ru, which correlates with the bulk calculations shown in Table 1.

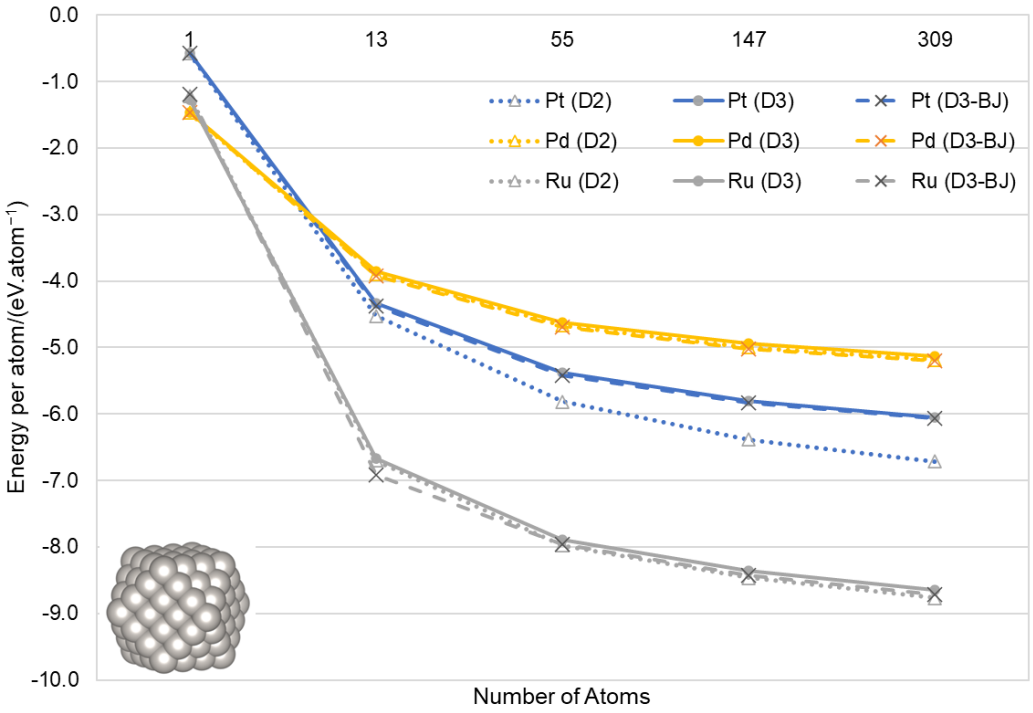

Figure 5. Energy per atom as a function of size for cuboctahedral Ru, Pd and Pt nanoparticles calculated with the three modelling methods, DFT-D2, DFT-D3 and DFT-D3(BJ).

The energies as a function of increasing sizes of the cubic nanoparticles of Ru, Pd and Pt, calculated by the three modelling methods, DFT-D2, DFT-D3 and DFT-D3(BJ), are shown in Figure 6. Again, the energy per atom increases as the nanoparticle size increases, with the surface-to-bulk atom ratio again decreasing from 12.00 to 3.85, 1.71, 1.13 and 0.82 for G_m = 13, 63, 171, 365 and 665, respectively. The number of bulk atoms exceeds the surface atoms at G_m = 665. Once again, the three calculation methods gave similar results for Pd and Ru, with the DFT-D2 method deviating for Pt. As expected, extrapolation to larger nanoparticles indicates that the energy per atom would again reach values above −5 eV/atom for Pd, −6 eV/atom for Pt and −8 eV/atom for Ru, which correlates with the bulk calculations shown in Table 1.

The most stable configurations in terms of energy per atom versus the number of atoms for spherical Ru, Pd and Pt nanoparticles of increasing sizes, calculated with the three DFT-D2, DFT-D3 and DFT-D3(BJ) modelling methods, are shown in Figure 7. Due to the incremental increase in radius of the theoretical spherical size considered, more structures were calculated. However, calculating the surface-to-bulk atom ratio is not the same as with the other nanoparticles, because each increment in size does not necessarily add a full shell to the particle. As expected, a decreasing trend of the surface-to-bulk ratio is still observed: 12.00, 18.00, 2.31, 3.23, 5.08, 0.58, 1.45, 1.56, 1.03, 0.49, 0.67 (0.84) and 0.60 for G_m = 13, 19, 43, 55, 79, 87, 135, 141, 177, 201, 255 (249) and 321, respectively. Surprisingly,

the overall energy per atom starts at a much higher energy than was observed for the other nanoparticles, but as in the other nanoparticles, the energies extrapolate to −5, −6 and −8 eV/atom for Pd, Pt and Ru, respectively.

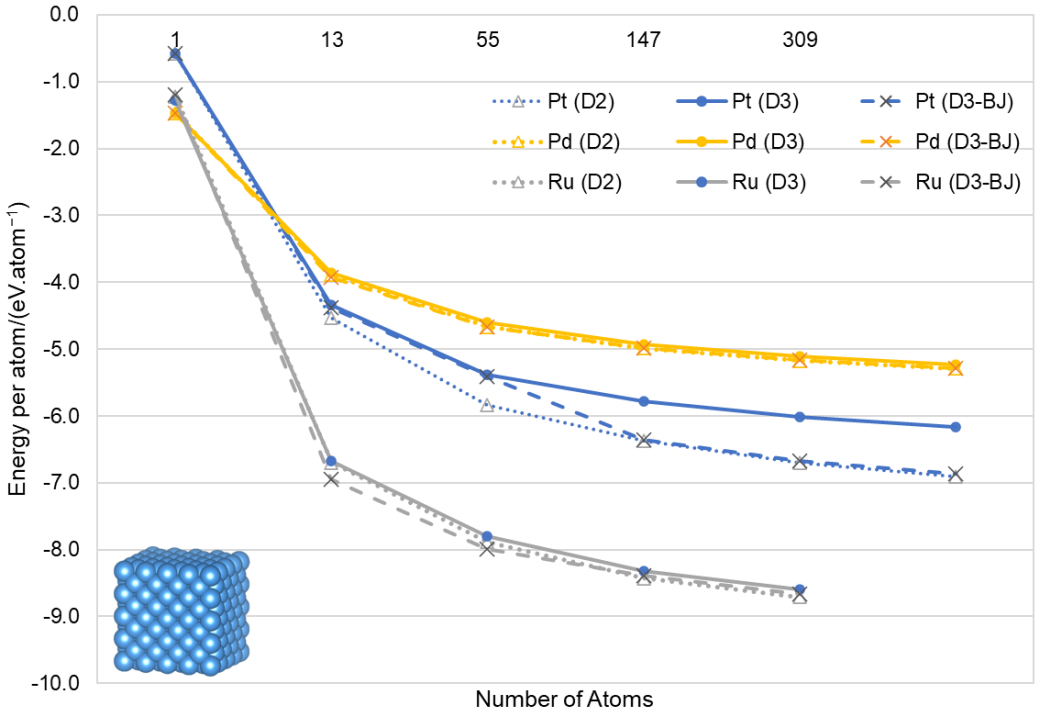

Figure 6. Energy per atom as a function of size for cubic Ru, Pd and Pt nanoparticles calculated with the three modelling methods, DFT-D2, DFT-D3 and DFT-D3(BJ).

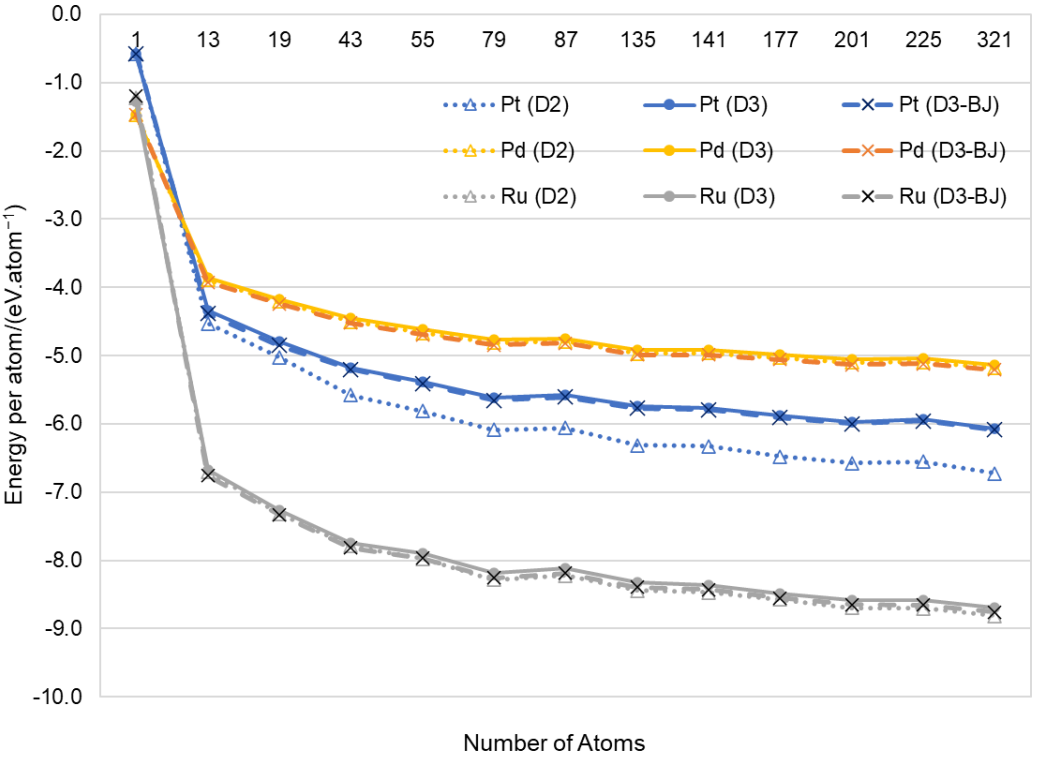

Figure 7. Energy per atom as a function of size for spherical Ru, Pd and Pt nanoparticles calculated with the three modelling methods, DFT-D2, DFT-D3 and DFT-D3(BJ).

Comparing the energy profiles for the five nanoparticle types, we can see that more than 200 atoms are needed before the energy per atom reaches the bulk energy for each respective metal type. It is also at this point that the number of bulk atoms matches or exceeds the surface atoms.

4. Conclusions

Density functional theory calculations have been employed to gain detailed understanding of the behaviour of different types of nanoparticles, compared to the *fcc* bulk metal and extended surfaces. It was determined that the DFT-D3(BJ) dispersion method provides the best agreement between calculated surface energies and lattice parameters compared to experimental values. Bulk, surface and nanoparticle calculations showed that the DFT-D2 method used for Pt overestimates the exchange correlation, leading to higher energy values that could erroneously suggest structures to be more stable than they are in reality.

The Wulff morphology of all three metal types showed that the (111) surface is the dominant surface but that the (001) and (011) surfaces are also expressed in the particle morphologies. However, when using the DFT-D3 method, the Pt nanoparticle only showed the presence of the (111) and (011) surfaces, indicating the sensitive balance between surface energies and the resulting morphologies.

Five different types of Ru, Pd and Pt nanoparticles of different sizes were considered, i.e., icosahedral, decahedral, cuboctahedral, cubic and spherical particles. Pt atoms at the surface moved into the bulk metal, leading to contraction that could explain the smaller nanoparticle sizes. Comparing the size of each metal, it was seen that Pt and Pd had similar sizes, with Ru being slightly larger. Overall, the energy per atom increases (becoming more negative) as the particle size increases and extrapolation to larger sizes indicates convergence to bulk energy values, irrelevant of the shape of the particular nanoparticle. The calculations showed that as soon as the surface-to-bulk ratio of the number of atoms is greater than one, the energy per atom resembles the bulk energies, which is a useful indication that only nanoparticles of smaller sizes need to be considered explicitly in calculations of their properties and behaviour, whereas it is likely that larger particles could be modelled accurately as a combination of bulk metal and extended surfaces.

Future work will include calculations of the interaction of hydrogen and small organic molecules with the nanoparticle surfaces, which should be directly comparable with experimental work. Our computational methods will allow the calculation of both the thermodynamics and kinetics of reaction pathways, thereby predicting likely products and identifying reaction mechanism, which will help the development of efficacious nano-catalyst shapes and sizes for experimental verification.

Author Contributions: Conceptualization, M.J.U. and N.H.D.L.; methodology, M.J.U.; software, M.J.U. and N.H.D.L.; validation, M.J.U.; formal analysis, M.J.U.; investigation, M.J.U.; resources, M.J.U. and N.H.D.L.; data curation, M.J.U.; writing—original draft preparation, M.J.U.; writing—review and editing, M.J.U. and N.H.D.L.; visualization, M.J.U.; supervision, N.H.D.L.; project administration, M.J.U. and N.H.D.L.; funding acquisition, N.H.D.L. All authors have read and agreed to the published version of the manuscript.

Funding: This research was funded by the Engineering and Physical Sciences Research Council (EPSRC grant No. EP/K009567/2).

Data Availability Statement: All data created during this research are openly available from Cardiff University's Research Portal: M.J. Ungerer and N.H. de Leeuw (2022). "Data for Computational Insights into Ru, Pd and Pt fcc Nano-Catalysts for Hydrogen Production Applications", Cardiff University's Research Portal, V. 1, Dataset. http://doi.org/10.17035/d.2022.0219184827 (26 September 2022).

Acknowledgments: We acknowledge the Engineering and Physical Sciences Research Council (EPSRC grant No. EP/K009567/2) for funding. This research was undertaken using resources of the Supercomputing Facilities at Cardiff University, UK, operated by ARCCA on behalf of Supercomputing Wales (SCW) projects, which is part-funded by the European Regional Development Fund

(ERDF) via Welsh Government. This work used the Isambard 2 UK National Tier-2 HPC Service (http://gw4.ac.uk/isambard/ (1 April 2021)) operated by GW4 and the UK Met Office, and funded by EPSRC (EP/T022078/1).

Conflicts of Interest: The authors declare no conflict of interest.

References

1. Petitpas, G.; Aceves, S. Hydrogen Storage in Pressure Vessels: Liquid, Cryogenic, and Compressed Gas. In *Hydrogen Storage Technology: Materials and Applications*; Klebanoff, L., Ed.; CRC Press: Boca Raton, FL, USA, 2016; pp. 91–108. ISBN 9781439841082.
2. Taube, M.; Rippin, D.; Cresswell, D.; Knecht, W. A System of Hydrogen-Powered Vehicles with Liquid Organic Hydrides. *Int. J. Hydrog. Energy* **1983**, *8*, 213–225. [CrossRef]
3. Amende, M.; Gleichweit, C.; Schernich, S.; Höfert, O.; Lorenz, M.P.A.; Zhao, W.; Koch, M.; Obesser, K.; Papp, C.; Wasserscheid, P.; et al. Size and Structure Effects Controlling the Stability of the Liquid Organic Hydrogen Carrier Dodecahydro-N-Ethylcarbazole during Dehydrogenation over Pt Model Catalysts. *J. Phys. Chem. Lett.* **2014**, *5*, 1498–1504. [CrossRef]
4. Schuster, R.; Bertram, M.; Runge, H.; Geile, S.; Chung, S.; Vonk, V.; Noei, H.; Poulain, A.; Lykhach, Y.; Stierle, A.; et al. Metastability of Palladium Carbide Nanoparticles during Hydrogen Release from Liquid Organic Hydrogen Carriers. *Phys. Chem. Chem. Phys.* **2021**, *23*, 1371–1380. [CrossRef] [PubMed]
5. Zhu, T.; Yang, M.; Chen, X.; Dong, Y.; Zhang, Z.; Cheng, H. A Highly Active Bifunctional Ru–Pd Catalyst for Hydrogenation and Dehydrogenation of Liquid Organic Hydrogen Carriers. *J. Catal.* **2019**, *378*, 382–391. [CrossRef]
6. Modisha, P.M.; Ouma, C.N.M.; Garidzirai, R.; Wasserscheid, P.; Bessarabov, D. The Prospect of Hydrogen Storage Using Liquid Organic Hydrogen Carriers. *Energy Fuels* **2019**, *33*, 2778–2796. [CrossRef]
7. Gall, D. Electron Mean Free Path in Elemental Metals. *J. Appl. Phys.* **2016**, *119*, 085101. [CrossRef]
8. Zhao, M.; Xia, Y. Crystal-Phase and Surface-Structure Engineering of Ruthenium Nanocrystals. *Nat. Rev. Mater.* **2020**, *5*, 440–459. [CrossRef]
9. Kusada, K.; Kobayashi, H.; Yamamoto, T.; Matsumura, S.; Sumi, N.; Sato, K.; Nagaoka, K.; Kubota, Y.; Kitagawa, H. Discovery of Face-Centered-Cubic Ruthenium Nanoparticles: Facile Size-Controlled Synthesis Using the Chemical Reduction Method. *J. Am. Chem. Soc.* **2013**, *135*, 5493–5496. [CrossRef]
10. Liu, L.; Corma, A. Metal Catalysts for Heterogeneous Catalysis: From Single Atoms to Nanoclusters and Nanoparticles. *Chem. Rev.* **2018**, *118*, 4981–5079. [CrossRef]
11. Cramer, C.J.; Truhlar, D.G. Density Functional Theory for Transition Metals and Transition Metal Chemistry. *Phys. Chem. Chem. Phys.* **2009**, *11*, 10757–10816. [CrossRef]
12. Viñ, F.; Gomes, J.R.B.; Illas, F. Chem Soc Rev Chemical Society Reviews Understanding the Reactivity of Metallic Nanoparticles: Beyond the Extended Surface Model for Catalysis. *Chem. Soc. Rev.* **2014**, *43*, 4922–4939. [CrossRef]
13. Nanda, K.K.; Maisels, A.; Kruis, F.E.; Fissan, H.; Stappert, S. Higher Surface Energy of Free Nanoparticles. *Phys. Rev. Lett.* **2003**, *91*, 106102. [CrossRef] [PubMed]
14. Kresse, G.; Hafner, J. Ab Initio Molecular Dynamics for Liquid Metals. *Phys. Rev. B* **1993**, *47*, 558–561. [CrossRef]
15. Kresse, G.; Hafner, J. Ab Initio Molecular-Dynamics Simulation of the Liquid-Metalamorphous- Semiconductor Transition in Germanium. *Phys. Rev. B* **1994**, *49*, 14251–14269. [CrossRef] [PubMed]
16. Kresse, G.; Furthmüller, J. Efficient Iterative Schemes for Ab Initio Total-Energy Calculations Using a Plane-Wave Basis Set. *Phys. Rev. B* **1996**, *54*, 11169–11186. [CrossRef]
17. Kresse, G.; Furthmüller, J. Efficiency of Ab-Initio Total Energy Calculations for Metals and Semiconductors Using a Plane-Wave Basis Set. *Comput. Mater. Sci.* **1996**, *6*, 15–50. [CrossRef]
18. Blöchl, P.E. Projector Augmented-Wave Method. *Phys. Rev. B* **1994**, *50*, 17953–17979. [CrossRef]
19. Kresse, G.; Joubert, D. From Ultrasoft Pseudopotentials to the Projector Augmented-Wave Method. *Phys. Rev. B* **1999**, *59*, 1758–1775. [CrossRef]
20. Perdew, J.P.; Burke, K.; Ernzerhof, M. Generalized Gradient Approximation Made Simple. *Phys. Rev. Lett.* **1996**, *77*, 3865–3868. [CrossRef]
21. Grimme, S. Semiempirical GGA-Type Density Functional Constructed with a Long-Range Dispersion Correction. *J. Comput. Chem.* **2006**, *27*, 1787–1799. [CrossRef]
22. Grimme, S.; Antony, J.; Ehrlich, S.; Krieg, H. A Consistent and Accurate Ab Initio Parametrization of Density Functional Dispersion Correction (DFT-D) for the 94 Elements H-Pu. *J. Chem. Phys.* **2010**, *132*, 154104. [CrossRef] [PubMed]
23. Grimme, S.; Ehrlich, S.; Goerigk, L. Effect of the Damping Function in Dispersion Corrected Density Functional Theory. *J. Comput. Chem.* **2011**, *32*, 1456–1465. [CrossRef] [PubMed]
24. Methfessel, M.; Paxton, A.T. High-Precision Sampling for Brillouin-Zone Integration in Metals. *Phys. Rev. B* **1989**, *40*, 3616–3621. [CrossRef] [PubMed]
25. Blöchl, P.E.; Jepsen, O.; Andersen, O.K. Improved Tetrahedron Method for Brillouin-Zone Integrations. *Phys. Rev. B* **1994**, *49*, 16223–16233. [CrossRef]

26. Huang, B.; Kobayashi, H.; Yamamoto, T.; Toriyama, T.; Matsumura, S.; Nishida, Y.; Sato, K.; Nagaoka, K.; Haneda, M.; Xie, W.; et al. A CO Adsorption Site Change Induced by Copper Substitution in a Ruthenium Catalyst for Enhanced CO Oxidation Activity. *Angew. Chem.* **2019**, *58*, 2230–2235. [CrossRef]
27. Hull, A.W. X-ray Crystal Analysis of Thirteen Common Metals. *Phys. Rev.* **1921**, *17*, 571–588. [CrossRef]
28. Corbel, G.; Topić, M.; Gibaud, A.; Lang, C.I. Selective Dry Oxidation of the Ordered Pt-11.1 at.% v Alloy Surface Evidenced by in Situ Temperature-Controlled X-ray Diffraction. *J. Alloy. Compd.* **2011**, *509*, 6532–6538. [CrossRef]
29. Monkhorst, H.J.; Pack, J.D. Special Points for Brillouin-Zon Integrations. *Phys. Rev. B* **1976**, *13*, 5188–5192. [CrossRef]
30. Song, C.; Sakata, O.; Kumara, L.S.R.; Kohara, S.; Yang, A.; Kusada, K.; Kobayashi, H.; Kitagawa, H. Size Dependence of Structural Parameters in Fcc and Hcp Ru Nanoparticles, Revealed by Rietveld Refinement Analysis of High-Energy X-ray Diffraction Data. *Sci. Rep.* **2016**, *6*, 31400. [CrossRef]
31. Arblaster, J.W. Crystallographic Properties of Platinum. *Platin. Met. Rev.* **1997**, *41*, 12–21. [CrossRef]
32. Arblaster, J.W. Crystallographic Properties of Platinum (Errata). *Platin. Met. Rev.* **2006**, *50*, 118–119. [CrossRef]
33. Watson, G.W.; Kelsey, E.T.; de Leeuw, N.H.; Harris, D.J.; Parker, S.C. Atomistic Simulation of Dislocations, Surfaces and Interfaces in MgO. *J. Chem. Soc. Faraday Trans.* **1996**, *92*, 433. [CrossRef]
34. Wulff, G., XXV. Zur Frage der Geschwindigkeit des Wachsthums und der Auflösung der Krystallflächen. *Z. Krist.* **1901**, *34*, 449–530. [CrossRef]
35. Rahm, J.; Erhart, P. WulffPack: A Python Package for Wulff Constructions. *J. Open Source Softw.* **2020**, *5*, 1944. [CrossRef]
36. Bhattarai, H.; Drisko, C.; Duraes, A.D.S.; Lin, T.; Charles, F.V., II; Christopher, J.; Fennell, M.A.M.; Louden, P.; Neidhart, S.; Kuang, S.; et al. *OpenMD-2.6: Molecular Dynamics in the Open*; University of Notre Dame: Notre Dame, Indiana, 2019.
37. Sutton, A.P.; Chen, J. Long-Range Finnis–Sinclair Potentials. *Philos. Mag. Lett.* **1990**, *61*, 139–146. [CrossRef]
38. Qi, Y.; Çağın, T.; Kimura, Y.; Goddard, W.A. Molecular-Dynamics Simulations of Glass Formation and Crystallization in Binary Liquid Metals: Cu-Ag and Cu-Ni. *Phys. Rev. B* **1999**, *59*, 3527–3533. [CrossRef]
39. Prasai, B.; Ren, Y.; Shan, S.; Zhao, Y.; Cronk, H.; Luo, J.; Zhong, C.J.; Petkov, V. Synthesis-Atomic Structure-Properties Relationships in Metallic Nanoparticles by Total Scattering Experiments and 3D Computer Simulations: Case of Pt–Ru Nanoalloy Catalysts. *Nanoscale* **2015**, *7*, 8122–8134. [CrossRef]
40. Prasai, B.; Ren, Y.; Shan, S.; Zhao, Y.; Cronk, H.; Luo, J.; Zhong, C.J.; Petkov, V. Correction: Synthesis-Atomic Structure–Properties Relationships in Metallic Nanoparticles by Total Scattering Experiments and 3D Computer Simulations: Case of Pt–Ru Nanoalloy Catalysts. *Nanoscale* **2015**, *7*, 10279. [CrossRef]
41. Momma, K.; Izumi, F. VESTA 3 for Three-Dimensional Visualization of Crystal, Volumetric and Morphology Data. *J. Appl. Crystallogr.* **2011**, *44*, 1272–1276. [CrossRef]
42. Ungerer, M.J.; Santos-Carballal, D.; Cadi-Essadek, A.; van Sittert, C.G.C.E.; de Leeuw, N.H. Interaction of H 2 O with the Platinum Pt (001), (011), and (111) Surfaces: A Density Functional Theory Study with Long-Range Dispersion Corrections. *J. Phys. Chem. C* **2019**, *123*, 27465–27476. [CrossRef]
43. Posada-Pérez, S.; Santos-Carballal, D.; Terranova, U.; Roldan, A.; Illas, F.; de Leeuw, N.H. CO2 Interaction with Violarite (FeNi2S4) Surfaces: A Dispersion-Corrected DFT Study. *Phys. Chem. Chem. Phys.* **2018**, *20*, 20439–20446. [CrossRef] [PubMed]
44. Lin, H.; Liu, J.X.; Fan, H.; Li, W.X. Compensation between Surface Energy and Hcp/Fcc Phase Energy of Late Transition Metals from First-Principles Calculations. *J. Phys. Chem. C* **2020**, *124*, 11005–11014. [CrossRef]
45. Wang, J.; Wang, S.Q. Surface Energy and Work Function of Fcc and Bcc Crystals: Density Functional Study. *Surf. Sci.* **2014**, *630*, 216–224. [CrossRef]
46. Singh-Miller, N.E.; Marzari, N. Surface Energies, Work Functions, and Surface Relaxations of Low-Index Metallic Surfaces from First Principles. *Phys. Rev. B Condens. Matter Mater. Phys.* **2009**, *80*, 235407. [CrossRef]
47. Tran, R.; Xu, Z.; Radhakrishnan, B.; Winston, D.; Sun, W.; Persson, K.A.; Ong, S.P. Surface Energies of Elemental Crystals. *Sci. Data* **2016**, *3*, 160080. [CrossRef]
48. Hulse, J.; Küppers, J.; Wandelt, K.; Ertl, G. UV-Photoelectron Spectroscopy from Xenon Adsorbed on Heterogeneous Metal Surfaces. *Appl. Surf. Sci.* **1980**, *6*, 453–463. [CrossRef]
49. Tyson, W.R. Surface Energies of Solid Metals. *Can. Metall. Q.* **1975**, *14*, 307–314. [CrossRef]
50. De Boer, F.R.; Boom, R.; Mattens, W.C.M.; Miedema, A.R.; Niessen, A.K. *Cohesion in Metals*; Elsevier Science Publishers: Amsterdam, The Netherlands, 1988.
51. Tyson, W.R.; Miller, W.A. Surface Free Energies of Solid Metals: Estimation from Liquid Surface Tension Measurements. *Surf. Sci.* **1977**, *62*, 267–276. [CrossRef]
52. Michaelson, H.B. The Work Function of the Elements and Its Periodicity. *J. Appl. Phys.* **1977**, *48*, 4729–4733. [CrossRef]
53. Caglar, B.; Kizilkaya, A.C.; Niemantsverdriet, J.W.; Weststrate, C.J. Application of Work Function Measurements in the Study of Surface Catalyzed Reactions on Rh(1 0 0). *Catal. Struct. React.* **2018**, *4*, 1–11. [CrossRef]
54. Tran, R.; Xu, Z.; Radhakrishnan, B.; Winston, D.; Sun, W.; Persson, K.A.; Ong, S.P.; Characteristic, S. The Inhibition of Epidermal Growth Factor Receptor Signaling by Hexagonal Selenium Nanoparticles Modified by SiRNA. *Cancer Gene Ther.* **2016**, *23*, 321–325. [CrossRef]
55. Lee, I.; Morales, R.; Albiter, M.A.; Zaera, F. Synthesis of Heterogeneous Catalysts with Well Shaped Platinum Particles to Control Reaction Selectivity. *Proc. Natl. Acad. Sci. USA* **2008**, *105*, 15241–15246. [CrossRef] [PubMed]

56. Shevchenko, V.Y.; Madison, A.E. Structure of Nanoparticles: I. Generalized Crystallography of Nanoparticles and Magic Numbers. *Glass Phys. Chem.* **2002**, *28*, 40–43. [CrossRef]
57. Mackay, A.L. A Dense Non-Crystallographic Packing of Equal Spheres. *Acta Crystallogr.* **1962**, *15*, 916–918. [CrossRef]
58. Ungerer, M.J.; Santos-Carballal, D.; Cadi-Essadek, A.; van Sittert, C.G.C.E.; de Leeuw, N.H. Interaction of SO2 with the Platinum (001), (011), and (111) Surfaces: A DFT Study. *Catalysts* **2020**, *10*, 558. [CrossRef]
59. Anderson, S.E.; McKay, B. Counting Polyhedra. Available online: http://www.numericana.com/data/polyhedra.htm (accessed on 1 June 2022).
60. Johnson, N.W. Convex Polyhedra with Regular Faces. *Can. J. Math.* **1966**, *18*, 169–200. [CrossRef]
61. Coxeter, H.S.M. 2.3 Quasi-Regular Polyhedra. In *Regular Polytopes*; Dover Publications: Dover, UK, 1973; pp. 18–19. ISBN 0-486-61480-8.
62. Farges, J.; De Feraudy, M.F.; Raoult, B.; Torchet, G. Noncrystalline Structure of Argon Clusters. I. Polyicosahedral Structure of ArN Clusters, 20 < N < 50. *J. Chem. Phys.* **1983**, *78*, 5067–5080. [CrossRef]
63. Farges, J.; de Feraudy, M.F.; Raoult, B.; Torchet, G. Noncrystalline Structure of Argon Clusters. II. Multilayer Icosahedral Structure of Ar N Clusters 50 < N < 750. *J. Chem. Phys.* **1986**, *84*, 3491–3501. [CrossRef]
64. Sloane, N.J.A.; Teo, B.K. Theta Series and Magic Numbers for Close-Packed Spherical Clusters. *J. Chem. Phys.* **1985**, *83*, 6520–6534. [CrossRef]
65. Vollath, D.; Fischer, F.D.; Holec, D. Surface Energy of Nanoparticles—Influence of Particle Size and Structure. *Beilstein J. Nanotechnol.* **2018**, *9*, 2265–2276. [CrossRef]
66. Kerber, T.; Sierka, M.; Sauer, J. Application of Semiempirical Long-Range Dispersion Corrections to Periodic Systems in Density Functional Theory. *J. Comput. Chem.* **2008**, *29*, 2088–2097. [CrossRef] [PubMed]